# Atomic environment of Fe following high-temperature implantation in InP

T. Cesca,* A. Gasparotto, G. Mattei, and V. Rampazzo
*INFM, Dipartimento di Fisica, Università di Padova, via Marzolo 8, I-35131 Padova, Italy*

F. Boscherini and B. Fraboni
*INFM, Dipartimento di Fisica, Università di Bologna, v.le Berti-Pichat 6/2, I-40137 Bologna, Italy*

F. Priolo
*INFM, Dipartimento di Fisica e Astronomia, Università di Catania, via S. Sofia 64, I-95123 Catania, Italy*

G. Ciatto and F. D'Acapito
*INFM-OGG, GILDA, c/o ESRF, Boîte Postale 220, F-38043 Grenoble Cedex, France*

C. Bocchi
*CNR-IMEM, Parco Area Delle Scienze 37/A, I-43100 Parma, Italy*

(Received 9 July 2003; revised manuscript received 15 October 2003; published 31 December 2003)

We report on the structural investigation of the atomic environment of Fe impurities introduced in InP by high-temperature ion implantation. The lattice location of the implanted Fe atoms and its evolution upon annealing treatments have been investigated by means of proton-induced x-ray emission and Rutherford backscattering spectrometry in channeling conditions. X-ray absorption spectroscopy measurements have been performed in order to study the Fe local structure. The results of these measurements have been correlated to those obtained with other structural characterization techniques, as transmission electron microscopy and high-resolution x-ray diffraction, and provide an overall picture of the Fe incorporation mechanisms at the atomic level. It has been found that the high-temperature implantation process favors the incorporation of Fe in high-symmetry sites. Conversely, the point defect flux occurring during high-temperature annealing controls the kick-out of the Fe atoms from substitutional locations, leading to the formation of Fe-P complexes.

DOI: 10.1103/PhysRevB.68.224113 PACS number(s): 61.72.Vv, 61.10.Ht, 61.82.Fk, 61.72.Yx

## I. INTRODUCTION

Among transition-metal impurities, iron is of key importance in the InP-based optoelectronic and microwave applications, thanks to its peculiar electronic and optical properties. Due to its near-midgap deep acceptor level Fe acts very efficiently as an electron trap,[1] and is therefore routinely used in bulk and epitaxial crystal growth to produce semi-insulating (SI) substrates or SI current blocking layers for vertical isolation and charge confinement in various device structures.[2–4] The same singly charged $Fe^{2+}$ trap state responsible for electrical compensation shows also interesting optical properties due to internal *d*-shell transitions between the $^5T_2$ and $^5E$ states whose degeneracy is removed by the InP tetrahedral crystal field;[1] these transitions give rise to a sharp photoluminescence spectrum centered at 3.5 $\mu$m which could be exploited to produce an emitting device in the mid-IR region.[5,6]

A major drawback of Fe-related applications is due to its rather low solubility in InP. This limits the maximum concentration of substitutionally located, electrically and optically active Fe atoms attainable with equilibrium techniques to values $\leqslant 10^{17}$ cm$^{-3}$ before precipitation occurs.[7–9] As a typical nonequilibrium technique, ion implantation may be used to overcome solubility limitations, and many papers appeared in the past dealing with the various aspects of the implantation process.[10–18] One of the problems with Fe implantation in InP is related to its high reactivity with the implant induced defects, especially when amorphous clusters or regions are produced:[19] the high-temperature annealing treatments necessary for the damage recovery induce strong redistribution/gettering phenomena which completely alter the implantation profile with detrimental effects on the desired electrical or optical properties. Damage-related undesired effects can be avoided by high-temperature implantation. Wendler *et al.*[20] showed that the formation of amorphous zones can be suppressed for doses as high as $10^{15}$–$10^{16}$ cm$^{-2}$ and medium mass ions (Si and Se) by keeping the InP substrate at temperatures above a critical value of the order of 400 K during the implantation; only residual isolated point defects and point defect clusters are left due to dynamical annealing effects inside the collision cascades. In some recent papers, by means of current-voltage, photoinduced current transient spectroscopy and photoluminescence and electroluminescence measurements,[21–23] we demonstrated that a concentration of electrically active iron of the order of $2\times10^{18}$ cm$^{-3}$ can be achieved by using an implantation temperature $T>200$°C; this active iron concentration, well above the Fe equilibrium solubility limit, is obtained without detrimental effects on the electrical, electronic, and optical properties of the $Fe^{2+}$ centers due to the implant induced damage.

Despite these important applicative results, several important questions of more fundamental character remain open and deserve careful investigation, mainly regarding the structural aspects of the ion-solid interaction. Presently, little or

 

no knowledge exists on the microscopic status of the crystal after the high-temperature implantation process and on the relationship between the host atoms, the produced defects, and the implanted Fe impurities. It would be of particular interest to know what is the effect of the dynamical annealing processes on the final location of the implanted Fe atoms and how the latter is modified by the following annealing treatments. Extracting information about the final site occupied by Fe could help, e.g., to understand why the electrically active Fe fraction after annealing treatments appears to be of the order of 10% only, as measured in the previously cited papers.[21,22]

The aim of this work is to study the structural relation between the InP crystal and the implanted Fe atoms after an elevated temperature ($T>200°C$) implantation process and the subsequent high-temperature annealing treatments. Thanks to the reduced damage rate during the implantation process, it is possible to introduce a relatively large amount of Fe without destroying the long-range crystallinity of the substrate and thus avoiding strong damage-related redistribution phenomena during the annealing: this allows to successfully employ structural techniques which otherwise suffer of sensitivity limitations (with respect, e.g., to the electrical/electronic ones) and to directly compare their results with those obtained by electrical measurements.

In order to obtain a clear picture of the structure of Fe implanted in InP on various length scales different techniques have been used. X-ray absorption spectroscopy (XAS) with synchrotron radiation was used to study the short-range environment of the implanted Fe atoms;[24,25] due to low concentration of the Fe absorber atoms, these measurements take full advantage of the high photon brilliance of third-generation synchrotron radiation sources. As the other main analytical tool we employed ion channeling of a proton beam, detecting backscattered protons (Rutherford backscattering spectrometry, RBS) as the matrix signal, to be compared with the Fe characteristic x-ray emission coming from the Fe impurities ionized by the beam (proton induced x-ray emission, PIXE). Other analytical tools were also employed to have an overall picture of the implantation process: these are secondary ion mass spectrometry (SIMS), transmission electron microscopy (TEM), and high-resolution x-ray diffraction (HRXRD). Thanks to the cross-related information obtained by the different techniques we will be able to propose a clear overall picture of the interaction of Fe with the InP lattice after implantation and as a consequence of the annealing process.

## II. EXPERIMENT

Czochralski *n*-doped (001) InP wafers were used as implantation substrates, both Sn and S doped, with background electron concentration in the $10^{18}\ cm^{-3}$ range. Samples were placed on a substrate holder kept at a temperature $T=220°C$ during implantation. Fe implants were performed at 350 keV at doses of $3\times10^{15}\ cm^{-2}$ (samples A) or $2\times10^{15}\ cm^{-2}$ (samples B), and at 300 keV with a $2\times10^{15}\ cm^{-2}$ dose (samples C). Four different dopings were employed for samples A: Sn $2\times10^{18}\ cm^{-3}$ (A1), Sn $5\times10^{18}\ cm^{-3}$ (A2), S $5\times10^{18}\ cm^{-3}$ (A3), and S $1\times10^{19}\ cm^{-3}$ (A4); a single doping was used instead for samples B and C, that is Sn $2\times10^{18}\ cm^{-3}$ and Sn $1\times10^{18}\ cm^{-3}$, respectively. Annealing was carried out for all the samples at a temperature $T=600°C$ for a time $t=90$ min in a tubular furnace with flowing purified $N_2$; the samples were placed in a small graphite boat where a phosphorus overpressure (generated by a saturated Sn:InP solution) was maintained in order to prevent surface decomposition due to P evaporation.[26] Samples B were annealed also at different temperatures from $T_{min}=300°C$ to $T_{max}=600°C$ for time intervals varying between $t=15$ min and $t=90$ min.

The evolution of the crystal damage was monitored by $^4He^+$ RBS channeling at energies between 1.8 and 2.2 MeV. Some selected samples were analyzed by cross-sectional TEM measurements with a FEI field-emission gun TECNAI F20 SuperTwin microscope, operating at 200 kV either in bright-field or high-resolution mode. Cross-sectional samples were prepared by mechanical prethinning followed by 6° incidence, 4-keV $Ar^+$ beam thinning on a Gatan PIPS system. Secondary ion mass spectrometry was used to determine the Fe depth profiles, using a 5.5-keV oxygen beam and detecting positive secondary ions. High-resolution x-ray diffraction experiments, using the (004) Bragg reflection, were carried out by means of a Philips X'Pert diffractometer equipped with a graded multilayer mirror and a Bartels channel-cut high-resolution monochromator for selecting the $CuK\alpha_1$ radiation. To reduce the background scattering coming from the sample, a thin slit was placed in front of the detector with an acceptance angle equal to nearly 0.3°; diffraction profiles were recorded in the $\omega-2\theta$ scan mode under controlled temperature conditions.

XAS measurements were performed at the ''GILDA'' (BM8) beamline of the European Synchrotron Radiation Facility in Grenoble, France. A sagitally focussing Si(311) monochromator run in the dynamical mode was used;[27] harmonics were rejected using a pair of Pd-coated grazing incidence mirrors and by detuning the crystals. The Fe absorption coefficient was monitored by recording the intensity of the Fe $K_\alpha$ line as a function of the exciting photon energy by using a thirteen-element hyperpure Ge detector with fast digital electronics. An Fe metallic foil and powder samples of $Fe_2O_3$ (hematite), $Fe_3O_4$ (magnetite), FeP, $Fe_2P$, and $Fe_3P$ were measured in the transmission mode as references for the XAS signal of Fe in different local environments. Extended x-ray absorption fine structure (EXAFS) spectra were recorded in the range 6950–8200 eV using an energy step providing an increment in *k* space smaller than 0.03 $Å^{-1}$. X-ray absorption near-edge structure (XANES) spectra were recorded in the range 7050–7250 eV, with an energy step as small as 0.1 eV in the range corresponding to the oxide preedge peaks and to the rising edge of bulk Fe, the Fe-P reference compounds and the samples.

Fe lattice location by PIXE channeling was carried out with a 1.85-MeV $H^+$ beam detecting the Fe $K_\alpha$ line at 6.4 keV with a Si(Li) detector. Complete angular scans across the $\langle100\rangle$ and $\langle110\rangle$ axial crystallographic directions were

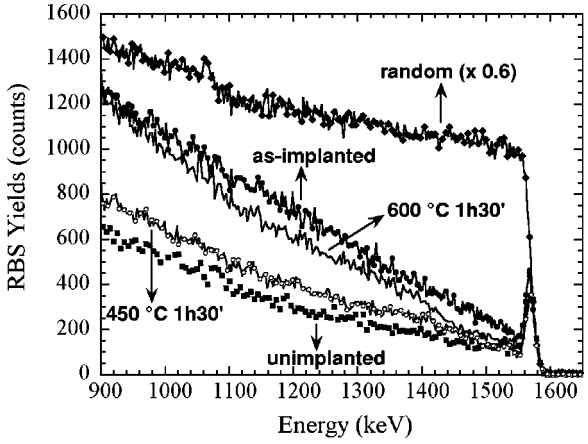


FIG. 1. RBS-channeling spectra ($^4He^+$ beam, 1.8-MeV energy) of 350-keV, $2\times10^{15}$ Fe/cm$^2$ implanted samples, both as-implanted and annealed at the different indicated temperatures for 90 min. The random reference spectrum is multiplied by the indicated factor for a better visualization.

performed for all the samples, recording the complete x-ray spectrum for each angular position. Control measurements along the $\langle 111\rangle$ axial and the three major planar directions were also performed to assess the exact location of Fe atoms. Proton backscattering spectra were recorded in parallel with each PIXE spectrum in order to compare the Fe and In angular yields; to rule out differences due to the dechanneling, the In signal was integrated from the surface over a thickness containing about 90% of the total implanted Fe. Each spectrum was recorded with the beam impinging on a fresh sample position to avoid damage accumulation effects. The angular scans around the various axes were performed with the beam remaining parallel to a fixed major planar direction, usually {100} or {110}.

## III. RESULTS

### A. Implant-induced lattice modifications

#### *1. As-implanted samples*

SIMS measurements show that the Fe implantation profiles have a projected range $R_p$ of 200 or 250 nm depending on the energy, with a peak concentration between 6 and 9 $\times10^{19}$ cm$^{-3}$ depending on the dose; the Fe concentration at the surface is in the range of $10^{19}$ cm$^{-3}$ for both doses, and the tail on the bulk side extends to a maximum depth of 1200-1500 nm.

In Fig. 1 we report the 1.8-MeV $^4He^+$ RBS-channeling results for some of the $2\times10^{15}$ cm$^{-2}$, 350-keV implanted and annealed samples. The as-implanted sample spectrum shows the presence of a diffuse dechanneling contribution throughout the entire implanted region, with only a moderate increase of the RBS yield with respect to the spectrum of an unimplanted reference sample; no direct scattering peaks, as would be caused by the presence of heavily damaged regions, are detected. TEM measurements (not shown) confirm the absence of detectable amorphous clusters, even if the implanted dose is almost two orders of magnitude higher

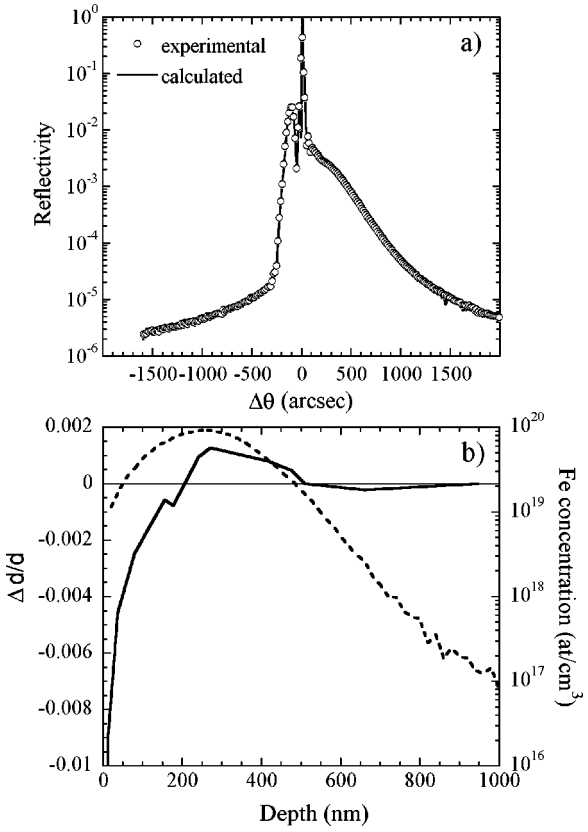


FIG. 2. (a) HRXRD experimental and simulated rocking curves of the 350-keV, $2\times10^{15}$ Fe/cm$^2$ as-implanted sample; (b) strain depth profile (continuous line, left-hand scale) and SIMS Fe implantation profile (dashed line, right-hand scale).

than the room-temperature amorphization threshold.[19,20] Moreover, increasing the dose from $2\times10^{15}$ to $3\times10^{15}$ cm$^{-2}$ does not modify the damage level detected by RBS. The depth distribution of the induced defects has been investigated by means of HRXRD; in Fig. 2 we report a rocking curve for the same as-implanted sample discussed above. Two distinct features are visible in the rocking curve [Fig. 2(a)]: a well-separated and rather sharp peak on the left of the main InP substrate peak and a more diffused increase of the reflectivity on the right side, with a tail extending to values of about 2000 arc sec from the central peak. These features clearly indicate the presence of two distinct contributions to the lattice deformation induced by the implantation: the peak on the left is associated with a positive strain, i.e., an expansion of the lattice parameter in a direction normal to the sample surface; the large shoulder on the right side is associated with a negative strain, i.e., a contraction of the lattice in the same direction. The experimental HRXRD curves were analyzed by means of a best fit procedure based on the standard dynamical diffraction theory for distorted crystals.[28,29] The subsurface region corresponding to the implantation depth was divided into several thin layers. The layer thickness $t$, the static Debye-Waller factor and the lattice spacing modification $\Delta d/d$ were the parameters of the calculations. In order to increase the quality of the fitting the experimental rocking curves were collected with a very high statistic within the whole angular range of measurement;

moreover, the incoherent diffuse scattering, due to thermal vibrations, was taken into account by introducing a suitable piecewise-smooth function. The diffuse scattering values were obtained by triple crystal diffractometry measurements in several points on the tails of the diffraction curves and then assumed as data points for the piecewise-smooth function. The reliability of the fitting results was also tested by repeating new calculations with very different starting conditions, in order to assure the convergence toward a global minimum. The result of the fitting is shown in Fig. 2(a), where an excellent agreement has been obtained between the experimental and calculated curves. The resulting $\Delta d/d$ profile is reported in Fig. 2(b), where it is compared with the as-implanted Fe depth distribution measured by SIMS. The presence of both lattice expansion and contraction is confirmed: lattice expansion is localized in a region between 200 and 500 nm, peaked in a position roughly corresponding to the maximum of the Fe implantation profile, whereas a large contraction effect is present in the near-surface region; a second region with negative strain contribution, though less evident than the one in the surface, is found at depths between 500 and 1000 nm, corresponding to the bulk tail of the Fe implantation profile.

#### *2. Annealed samples*

The RBS spectra of annealed samples (see Fig. 1) show that the defect recombination induced by the thermal treatments leads to a good crystal reconstruction already at an annealing temperature of 450°C, with an almost complete recovery in the near-surface region. For the 600°C annealed sample an increase of the channeling yield is visible in a region corresponding to depths between about 170 and 350 nm, very likely due to the onset of extended defects. Again, similar results are obtained for the samples implanted at the $3\times10^{15}$ cm$^{-2}$ dose, without a significant increase of the secondary defect production. The onset of extended defects after annealing at the highest temperatures is confirmed by cross-sectional TEM observation, as reported in Fig. 3 for a $3\times10^{15}$ cm$^{-2}$ implanted sample annealed at 600°C: this image shows the formation of a band of extended defects in a region starting at a depth of about 200 nm and extending up to several hundred nanometers. Most of these defects appear very similar to the ones detected and studied in room-temperature implanted InP samples:[19,30] though a detailed analysis of these defects is beyond the scope of this article, they are very likely extrinsic dislocation loops [see Fig. 3(b)] due to the condensation of the excess interstitials produced by the implant which survived the recombination process with vacancies. The SIMS measurements (not reported here, see Ref. 31) show that the implanted Fe profiles do not undergo severe modification upon annealing. The 450°C annealed sample profile is identical to the as-implanted sample one; after the 600°C annealing a minor redistribution effect is observed in the region between the surface and the projected range $R_p$, with a plateau visible in the near-surface region and a small peak centered at around $R_p/2$. No Fe gettering phenomena due to secondary defect formation observed at greater depths are visible from SIMS profiles. Figure 4 reports the HRXRD results for the 350-keV, $2\times10^{15}$ cm$^{-2}$ implanted sample annealed at 600°C. An overall reduction of the strain with respect to the as-implanted sample is already evident from a simple inspection of the rocking curve [Fig. 4(a)]. The strain profile [Fig. 4(b)] shows two contributions to the lattice expansion ($\Delta d/d>0$) at different depth, separated by a region with a clearly distinguishable lattice contraction ($\Delta d/d<0$). An hypothesis about the possible origin of this particular strain profile will be presented in the discussion section.

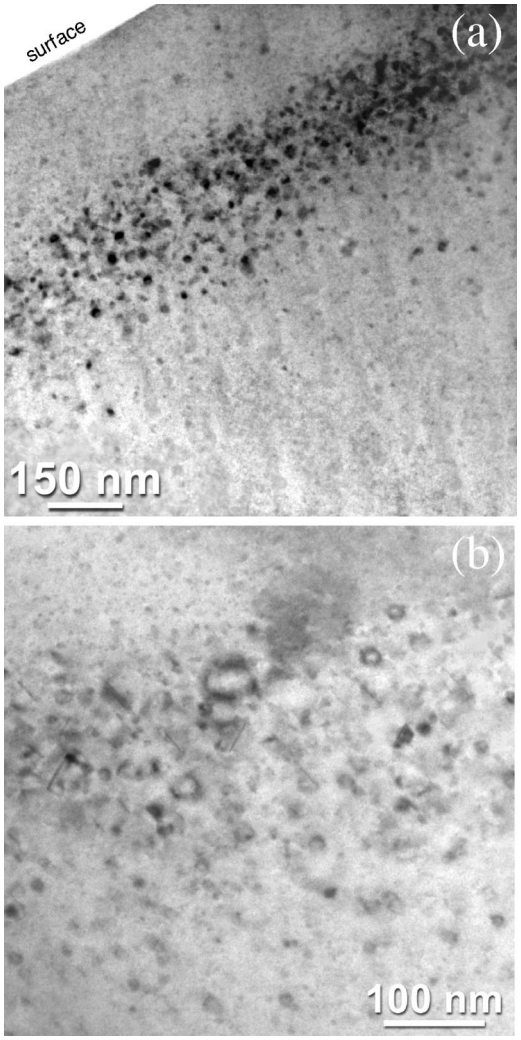


FIG. 3. (a) Cross-sectional bright-field TEM image of a 350-keV, $3\times10^{15}$ Fe/cm$^2$ implanted sample, annealed at $T=600$°C for 90 min; (b) enlargement in the damaged region; the image is taken at a different tilt angle and dislocations and dislocation loops become clearly visible.

### B. Fe local environment: XAS measurements

In Fig. 5 we report XANES spectra of four selected samples compared with those of three reference Fe-P compounds, bulk Fe and two iron oxides. The preedge background was subtracted using a linear function and the spectra were normalized to a common value at 7250 eV. As expected on the basis of the charge transfer on the Fe absorbing atom, and extensively reported in the literature,[32,33] the position of

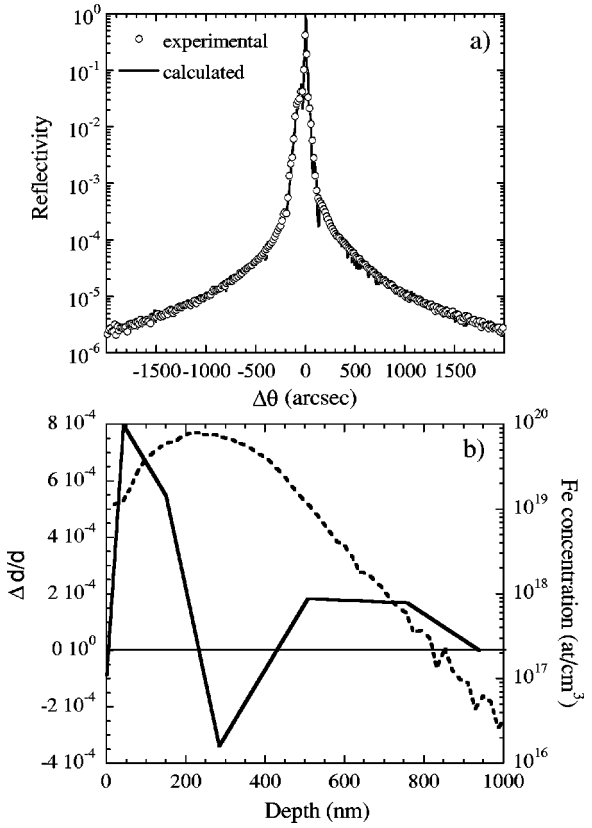


FIG. 4. (a) HRXRD experimental and simulated rocking curves of the 350-keV, $2\times10^{15}$ Fe/cm$^2$ annealed sample; (b) strain depth profile (continuous line, left-hand scale) and SIMS Fe implantation profile (dashed line, right-hand scale).

the absorption edge in the spectra of the two oxides is significantly shifted towards higher energy with respect to metallic Fe. The spectra of the four samples have inflection points significantly lower in energy than those of the oxides (by $\sim$5 eV): this excludes that Fe in the samples is present in significant fraction in the form of oxides. Moreover, the comparison of the overall line shape of the sample spectra with that of bulk Fe indicates that iron is not present in the metallic form in the samples. A comparison of the sample spectra with those of the three Fe-P compounds is more problematic and provides less direct information. While an overall similarity can be observed, it is difficult to establish whether the spectrum of any of the samples is similar to one particular Fe-P compound. Only some qualitative remarks can be made. There are noticeable changes between the spectra of as-implanted and annealed compounds. The double-peak structure in the range 7130–7145 eV in the as-implanted samples is filled, forming a single oscillation as in FeP, in the annealed ones; at the same time, the rising edge (7110–7120 eV) of the spectra becomes more structured, with a sharper step, upon annealing, as in $Fe_2P$ and in FeP. These observations suggest that upon annealing the local coordination of Fe becomes similar to that present in the FeP compound. An intense preedge feature in the XANES spectra of 3*d* metals is a well known signature of the presence of metallic atoms in tetrahedral symmetry; the peak at $\sim$7114 eV in magnetite has this origin. No such prepeak can be observed in the

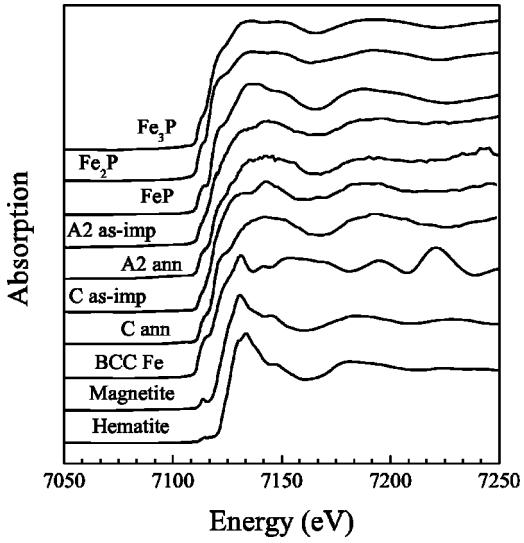


FIG. 5. XANES spectra of four selected samples, as-implanted (A2 as-imp, C as-imp) and annealed at 600°C for 90 min (A2 ann, C ann) compared with those of three Fe-P compounds, bulk Fe and two iron oxides.

sample spectra. However, the comparison between spectra of oxide and phosphide compounds is not straightforward. In fact it is probable that, due to bonding arrangements and charge-transfer different from the oxides, bound and continuum state transitions overlap in Fe-P compounds. Therefore, the absence of a prepeak in the XANES of the implanted samples cannot be taken as a demonstration of the absence of Fe sites with tetrahedral symmetry.

EXAFS data were quantitatively analyzed with the AUTOBK and FEFFIT programs[34,35] using theoretical phase signals generated by FEFF 8.0.[36] Raw absorption data were background subtracted using the AUTOBK routine. Despite the low concentration of the absorber atom the spectra are of sufficient quality to obtain first shell information. In Fig. 6

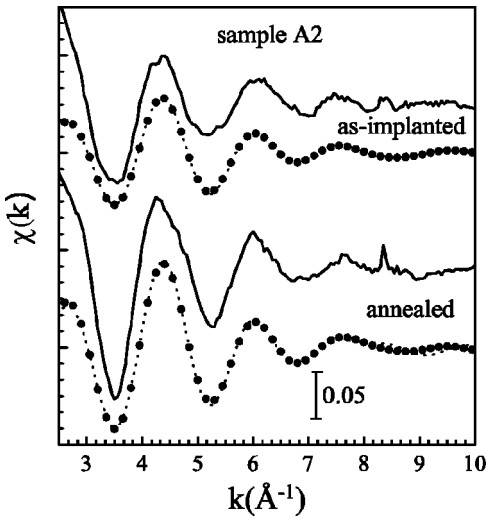


FIG. 6. Selected EXAFS data for sample A2, as-implanted and annealed at 600°C for 90 min: raw data (continuous line), filtered first shell contribution (dashed line), fit (dots).

TABLE I. Quantitative results of the fitting procedure for the Fe-P first shell: coordination numbers (CN), mean square relative displacements ($\sigma^2$), and interatomic distance ($R$).

| Sample | CN | $\sigma^2$ ($10^{-3}$ Å$^2$) | $R$ (Å) |
|---|---|---|---|
| As-implanted | | | |
| A2 | 4.4±0.6 | 7.9±3.2 | 2.354±0.017 |
| A3 | 3.9±0.6 | 6.5±3.9 | 2.367±0.020 |
| A4 | 4.3±0.4 | 6.9±2.3 | 2.346±0.012 |
| C | 3.6±0.4 | 4.5±2.3 | 2.386±0.013 |
| Annealed | 600°C 90 min | | |
| A1 | 6.4±0.8 | 7.7±3.2 | 2.351±0.016 |
| A2 | 6.9±0.8 | 9.3±2.9 | 2.348±0.015 |
| A3 | 6.1±0.8 | 7.2±3.1 | 2.340±0.018 |
| A4 | 5.6±0.7 | 7.4±3.2 | 2.338±0.017 |
| C | 5.8±0.9 | 8.1±3.6 | 2.375±0.019 |

we report the raw data, the filtered first shell contributions and the fits of a selected sample (A2), as-implanted and annealed. Similar results were obtained for all the investigated samples. Qualitative inspection shows only a single frequency signal to be present. The envelope of oscillations decreases rapidly as a function of the wave vector $k$, suggesting bonding with a low-$Z$ element; moreover, a systematic increase in the EXAFS amplitude can be observed in the spectra of annealed samples with respect to those of the as-implanted ones. The presence of a single frequency is confirmed by analysis of the Fourier transforms (not shown here, see Ref. 37) and the hypothesis that the EXAFS signal is due to a low-$Z$ element is in agreement with the previously described analysis of the XANES spectra. The spectra were fitted in the $R$ range 0.9 to 2.6 Å and in the $k$ range 2.8 to 10 Å$^{-1}$, using a $k^0$ weight and a single Fe-P signal. The fitting parameters were the interatomic distance, the mean square relative displacement ($\sigma^2$), the coordination number (CN), and an energy origin shift; the many-body amplitude reduction factor was fixed to the value found from analysis of the FeP standard compound. The results of the quantitative analysis are summarized in Table I (reported errors are purely statistical and correspond to $1\sigma$ in the fitted parameter).

The main difference in the local structural parameters is a systematic increase in the Fe-P CN upon annealing. While it is difficult to propose a unique structural model and it is highly probable that in these sample Fe is present in a number of different local configurations, the values for the CN suggest that in the as-implanted samples Fe is predominantly in a local configuration with a CN close to 4 and that annealing induces a transition to a CN close to 6. A CN equal to 4 would be found for a substitutional or an interstitial Fe in the InP lattice while a CN equal to 6 would be found in local structures similar to FeP or $FeP_2$. In all cases the structures are not ordered beyond the first coordination shell. The values of the first shell $\sigma^2$ do not vary much and are constant at moderately high levels. The interatomic distances determined from the fit are close to Fe-P bond lengths in FeP or $FeP_2$, which range between 2.243 and 2.350 Å,[38,39] and also to the sum of the covalent radii of Fe and P. These local structural parameters are consistent with the XANES lineshape analysis.

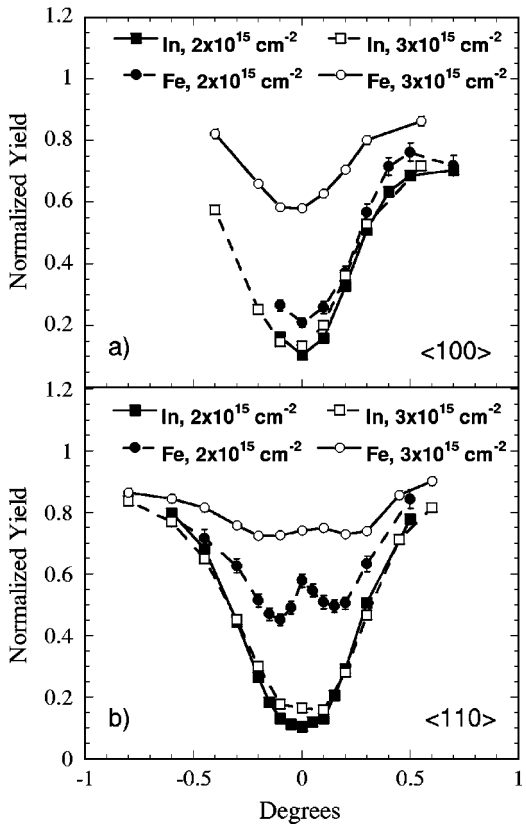


FIG. 7. ⟨100⟩ (a) and ⟨110⟩ (b) channeling dips of 350-keV, $2\times10^{15}$ and $3\times10^{15}$ Fe/cm$^2$ as-implanted samples.

A detailed high-resolution TEM (HRTEM) investigation has been performed on sample A4 (350 keV, $3\times10^{15}$ Fe/cm$^2$, annealed at 600°C for 90 min) in the region where secondary extended defects have been revealed (see Fig. 3), that is in the Fe implant peak region. The images have shown Moiré fringes induced by inclusions in the crystalline matrix. The fast Fourier transform analysis of these regions in comparison with that obtained from the host InP matrix has demonstrated that these inclusions are originated by local distortions at small angles of the InP matrix and no reflection from an Fe-P phase has been revealed; moreover, no other structures (neither amorphous nor crystalline) possibly associated with Fe-containing precipitates or complexes are visible by HRTEM.

### C. Fe lattice position: PIXE-channeling results

Most of the channeling measurements were performed on the 350-keV implanted samples (samples A and B). The main results of angular scans (also named ''channeling dips'' in the following) performed around ⟨100⟩ and ⟨110⟩ axes for the 350-keV as-implanted samples are presented in Fig. 7. The In and Fe yields $\chi_{In}$ and $\chi_{Fe}$ as a function of the angular coordinate from the axes are reported; the yield $\chi$ is normalized to the random yield obtained by a circular scan performed around the axial coordinate. A simple qualitative in-

spection of the dips reveals that for both the implanted doses channeling strongly affects the Fe angular yield behavior. An evident minimum is observed at the channel center for the $\langle 100 \rangle$ axis, whereas a more structured situation is visible for the $\langle 110 \rangle$ case, with an evident peak superimposed to the minimum at the channel center. Control scans performed along the $\langle 111 \rangle$ direction (not shown) show a single minimum dip structure similar to the one detected for the $\langle 100 \rangle$ axis. The intensities of both the observed minimum and the central peak decrease with increasing dose, but the effect is still clearly present for the $3\times10^{15}$ cm$^{-2}$ implanted sample. The decrease of the yield moving from the planar alignment towards the channel center for all the three directions indicates that a significant fraction of the Fe atoms is aligned with the crystal rows and is therefore prevented from having close-encounter collisions with the channeled beam. This means that this fraction of Fe atoms occupies positions of well-defined high symmetry in the InP host lattice after implantation. For the zincblende structure these positions can be either substitutional or tetrahedral interstitial sites.[40,41] The significantly higher Fe yield observed for the $\langle 110 \rangle$ perfect alignment is a clear indication that part of the Fe atoms, aligned with the $\langle 100 \rangle$ and $\langle 111 \rangle$ crystal rows, occupy tetrahedral interstitial sites and are not shadowed by the $\langle 110 \rangle$ rows. The evident peak at the channel center is due to the beam flux enhancement effect known as ''flux peaking'' (see, for example, Refs. 42,43); a single peak at the channel center is expected due to tetrahedral interstitials, as we performed most of the angular scans with the beam parallel to the $\{100\}$ planar direction.[41] This picture is confirmed also by angular scans performed across the major planar crystal directions, taking into account that tetrahedral interstitials in zincblende structure are shadowed in both $\{100\}$ and $\{110\}$, but not in $\{111\}$ planar alignment.

In order to extract quantitative information from the dips we have to compare the In and Fe yields as explained in the following. The basic assumption is that for 100% alignment of the Fe atoms with the crystal rows the In and Fe yields will be equal, as will be the relative channeling dips. For dips with a single minimum at the channel center, as in the case of the $\langle 100 \rangle$ angular scans, we can evaluate the fraction $f_A$ of Fe atoms aligned with the axial row from the minimum yields using the known Feldman expression.[44] The remaining fraction $f_R = 1 - f_A$ gives the number of Fe atoms which are not shadowed by the crystal rows in all the axial directions and are therefore randomly distributed within the crystal (random fraction). The fraction $f_A$ calculated from the $\langle 100 \rangle$ (or equivalently from $\langle 111 \rangle$) dips contains atoms positioned both in substitutional and tetrahedral interstitial sites. To estimate the relative weight of the two site occupancies we have to analyze the $\langle 110 \rangle$ channeling dips. We start from the phenomenological expression proposed by Yu *et al.*[40] for the yield at the $\langle 110 \rangle$ channel center, which takes into account the flux peaking effect. The normalized Fe yield can be written as

$$\chi_{Fe} = f_R + f_A[Fx + \chi_{\mathrm{In}}(1-x)], \tag{1}$$

where $x$ represents the fraction of $\langle 100 \rangle$ aligned iron atoms which are actually located in tetrahedral interstitial sites,

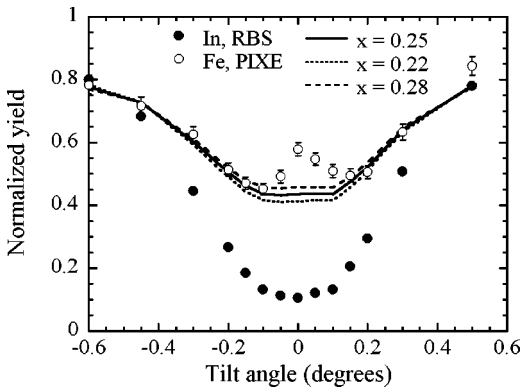


FIG. 8. $\langle 110 \rangle$ channeling dip of the 350-keV, $2\times10^{15}$ Fe/cm$^2$ as-implanted sample. The continuous line represents the best result achieved by using Eq. (3); the values of $x$ are reported in the legend and $\sigma = 1.3°$ is used.

while $(1-x)$ indicates the portion of $\langle 100 \rangle$ aligned iron atoms which occupy substitutional positions. The contribution of the interstitials is multiplied by the factor $F$, the flux peaking parameter: it is a number $\geqslant 1$ and represents the enhancement effect of the nonuniform beam flux distribution inside the channel. The exact value of $F$ cannot be easily determined *a priori*: from channeling simulations of surface layers (100 nm) in a diamond cubic lattice Bech Nielsen *et al.*[43] estimated a value between 1.8 and 2.2. The exact value and the shape of the resulting peak is influenced by the experimental conditions and in particular by the dechanneling; taking into account this effect, Yu *et al.*[40] estimated a value of $F$ between 1.5 and 1.7 for a 5-$\mu$m thick layer in InP. We therefore prefer to try to reproduce the overall shape of our channeling dips *excluding* the flux peaking peak region. By imposing $F = 1$ we may use Eq. (1) to represent the iron yield curve as a function of the angular coordinate $\psi$ in the hypothesis of a uniform beam flux across the channel: the complete $\langle 110 \rangle$ indium dip $\chi_{\mathrm{In}}$ is used to model the shape of the Fe dip, which is related to the substitutional atoms. However, in this way the iron atoms in tetrahedral interstitial sites are treated as if they contributed to the random fraction in the whole range of angular coordinates. This is strictly correct only for the central point of the dip, whereas the interstitial iron contribution rapidly decreases when moving away from the $\langle 110 \rangle$ axis towards the $\{100\}$ plane. In fact, a better agreement with the experimental curve is obtained if we use, instead of a constant $F$ value, an angular dependent parameter $p(\psi)$ varying between 1 and 0, defined as follows:

$$p(\psi) = 1 - \frac{1}{\sigma}|\psi|, \tag{2}$$

where $\sigma$ is an adjustable parameter of the order of the channeling dip width; best results are obtained for a value of $\sigma \approx 1°$. With this position, Eq. (1) assumes the following aspect:

$$\chi_{\mathrm{Fe}} = f_R + f_A[p(\psi)x + \chi_{\mathrm{In}}(1-x)]. \tag{3}$$

The result of this procedure for the $2\times10^{15}$ cm$^{-2}$, 350-keV as-implanted sample is shown in Fig. 8. The resulting angu-

lar curves are shown for three different values of $x$, showing also the sensitivity of the method in determining the values of $x$. This procedure was applied to all the $\langle 110 \rangle$ channeling dips of the different samples implanted at 350 keV to extract the values of the substitutional and tetrahedral interstitial fractions. It has to be pointed out that, whereas the random and aligned fractions values $f_R$ and $f_A$ are directly calculated from experimental results and are therefore exact within experimental errors, the interstitial and substitutional fractions derived from the above described procedure are only indicative of the relative consistency of the two site populations. Anyhow, a further check can be done by calculating *a posteriori* the value of the flux peaking parameter $F$ from the difference between experimental and calculated curves at the center of the $\langle 110 \rangle$ channel, where we assumed $F=1$. Resulting values of $F$ are in the range from 1.7 to 2.2, in good agreement with the previously cited values of Bech Nielsen *et al.*

The quantitative results obtained with this procedure show that a high fraction of the Fe atoms reside on high-symmetry sites after implantation in the as-implanted samples: $84(\pm 5)\%$ for the $2\times10^{15}$ cm$^{-2}$ and $48(\pm 3)\%$ for the $3\times10^{15}$ cm$^{-2}$ dose. Most of these atoms are substitutionally located, whereas a minor fraction (about 10–20%) occupies tetrahedral interstitial sites. The remaining Fe atoms are randomly distributed throughout the InP lattice, without preferential positions. The fraction of randomly distributed Fe atoms appears to increase with the implantation dose, leading to a saturation of the total substitutional Fe content to a value of $\sim 1.2\times10^{15}$ cm$^{-2}$. It is worth noting that this value corresponds to a substitutional Fe peak concentration of about $3\times10^{19}$ cm$^{-3}$, which is $\sim$300 times higher than the equilibrium Fe solubility limit in InP. The situation is radically changed after high-temperature annealing treatments: the angular scans performed on the $3\times10^{15}$ cm$^{-2}$ implanted samples (samples A) annealed at 600°C for 90 min (not reported here, see Ref. 45) show a nearly uniform yield across the entire channel width for both $\langle 100 \rangle$ and $\langle 110 \rangle$ directions, indicating that most of Fe atoms left their substitutional or tetrahedral interstitial positions during the thermal treatment and are randomly oriented with respect to the host InP lattice. The effect of the annealing on the site occupancy of the Fe atoms is displayed in Fig. 9, where we show, as a function of the annealing temperature, the substitutional, tetrahedral interstitial, and randomly distributed Fe fractions evaluated from the channeling dip analyses for the $2\times10^{15}$ cm$^{-2}$ implanted samples (samples B). For temperatures lower than 400°C the situation is only slightly modified with respect to the as-implanted sample, with a high substitutional Fe concentration and a rather constant amount of tetrahedral interstitial iron. Between 400 and 450°C the substitutional concentration starts to decrease while the random fraction increases; at higher temperatures the Fe atoms lose progressively their substitutional locations in favor of random locations, until the concentration of randomly located iron reaches 100% for the highest annealing temperature. On the other hand, the fraction of tetrahedral interstitial iron remains approximately constant for temperatures between 400 and 550°C, showing only a slight decrease between 350 and 400°C; this behavior of both the substitutional and tetrahedral fractions is in analogy with the results obtained by Wahl and co-workers[46] in emission channeling studies on Cu and Ag implanted Si. At an annealing temperature $T_{ann}=600$°C it appears that, for both the implanted doses, iron has been completely removed from substitutional sites, or it is present at these locations in concentration below the sensitivity of our technique (between 5 and 10%). Similar measurements performed on samples B, annealed for 15 min at the same temperatures, show a very similar behavior, with only slightly higher values of the aligned fraction with respect to the 90-min annealed samples. This suggests that the annealing temperature dominates the dynamic of the Fe incorporation in the InP lattice sites, with a minor role played by the annealing duration.

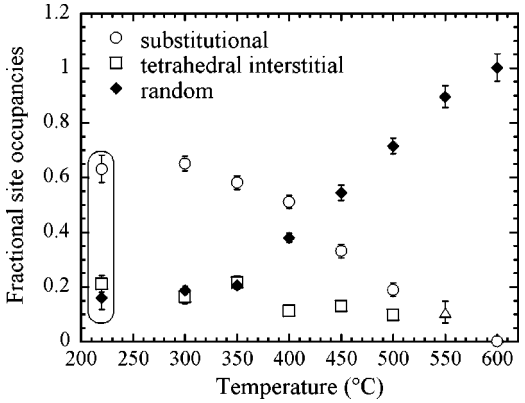


FIG. 9. Substitutional, tetrahedral interstitial, and random Fe fractions as a function of the annealing temperature for the 350-keV, $2\times10^{15}$ Fe/cm$^2$ implanted samples (B series), evaluated from the analysis of the PIXE-channeling dips; the annealing treatments are performed at the various temperatures for 90 min. The frame encloses the results of the as-implanted sample. The value at $T=550$°C (open triangle) represents the resulting $\langle 100 \rangle$ aligned fraction: due to measurement uncertainties it is not possible to discriminate between the substitutional and tetrahedral interstitial fractions from the analysis of the corresponding channeling dip.

## IV. DISCUSSION

The investigation of the crystal damage in our implanted samples performed by RBS-channeling and TEM measurements have shown that the increased defect mobility inside the primary collision cascade due to the elevated implantation temperature locally favors the vacancy-interstitial recombination; this causes a strong reduction of the total damage production in the as-implanted samples and the residual damage mostly consists of isolated point defects and/or point defect clusters, in agreement with the results of Wendler *et al.*[20] Moreover, the effect is independent of the Fe dose, again in accordance with the presence of a plateau in the damage vs ion dose curve reported by Wendler. At the same time, the limited damage production, together with the availability of implant-induced vacant sites, favors the incorporation of the implanted Fe atoms in substitutional In positions. This has been confirmed by the results on the Fe lattice location obtained by PIXE-channeling measurements which

indicate that substitutional Fe densities more than two orders of magnitude above the Fe solubility limit in InP can be achieved in the as-implanted samples. XAS measurements have also provided a cross-validation to this high degree of substitutionality demonstrating that Fe is fourfold coordinated with the P atoms in the as-implanted samples, as it occurs for Fe occupying substitutional or tetrahedral interstitial sites in the InP lattice.

These results are consistent with the features visible in the HRXRD curve of the as-implanted sample (Fig. 2). The simultaneous presence of both lattice expansion and contraction and their different depth distribution are in agreement with the different depth distribution of vacancies and interstitials produced during the implant.[47–49] In particular for ion implantation in InP, Christel and Gibbons[48] have shown that due to the forward momentum transfer to the recoiling atoms an excess of vacancies exists at shallow depths in the implanted samples, while excess interstitials are present at greater depths, in the implant peak region; both have peak concentrations of the same order of magnitude of the implantation profile peak. In our case, as previously remarked, thanks to dynamical annealing effects occurring during the high-temperature implants most of the vacancies and interstitials locally recombine; nonetheless, due to the kinetics of the defect production, it is very likely that the remaining point defects follow the above mentioned depth distribution: excess vacancies are left behind in the near-surface region, while excess interstitials are present in proximity of the Fe peak. The different defect distribution gives rise to lattice deformations of opposite sign in two distinct regions: a lattice contraction where vacancies dominate and a lattice expansion where interstitials prevail. This explains the features visible in Fig. 2(b) in the near surface and the iron peak regions. Conversely, the negative strain contribution visible in the region corresponding to the bulk tail of the iron profile cannot be anymore attributed to the presence of excess vacancies, whose concentration is negligible at those depths. A possible explanation is instead related to the presence of high concentrations of iron atoms occupying substitutional positions, as revealed by PIXE and XAS. The idea is based on atomic size considerations: the ionic radius of Fe in the $Fe^{3+}$ state (0.64 Å) is smaller than the ionic radius of In (0.81 Å) and a contraction of the lattice parameter may occur when an Fe atom substitutes for an In atom, inducing a negative strain component. Such an effect is visible only at depths corresponding to the Fe implant tail where the concentrations of excess vacancies and excess interstitials are negligible and do not contribute significantly to the strain.

The situation radically changes upon annealing. The temperature evolution of the extended defect formation (Fig. 1) and the annealing behavior of the Fe site occupation (Fig. 9) suggest a correlation between these two phenomena. The postimplantation thermal treatments favor the recombination of the implant-induced vacancies and interstitials and a good crystal recovery can be obtained for $T \geqslant 450°C$. At the highest annealing temperatures the interstitials gain enough mobility to coalesce and form secondary extended defects, as directly observed by TEM (Fig. 3). Correspondingly, the increase of the annealing temperature above 450°C results in an increase of the randomly located Fe fraction to the detriment of the substitutional occupation and at 600°C almost all the Fe atoms have moved out from high-symmetry sites. This situation is similar to the one observed by Pearton and coworkers for GaAs implanted with shallow dopant ions.[50] An increased Fe mobility is expected due to the increase of the point defect mobility observed at high annealing temperatures. This is confirmed by SIMS measurements which showed that a slight Fe redistribution occurs in the 600°C annealed sample, in the region between the sample surface and the projected range $R_P$, which is the region where the most intense interstitial-vacancy flux during point defect recombination occurs. These results indicate that the high concentrations of interstitials produced during the implant and their high mobility, which at the highest temperatures causes the formation of extended defects, may be responsible of both the Fe redistribution phenomena and the escape process of the Fe atoms from high-symmetry locations. Several works reported in the literature indeed confirm that iron diffuses in InP via a kick-out mechanism mediated by mobile interstitials.[51,52] Nonetheless, after their escape from the high-symmetry positions the Fe atoms do not diffuse inside the samples. The SIMS measurements clearly show that the Fe profiles are stable upon annealing even at the highest temperatures: the previously discussed Fe redistribution occurring in the 600°C annealed sample confirms the dominant role of the interstitials in the kick-out process of the Fe atoms but it also shows that it is not quantitatively relevant. An explanation to the limited Fe mobility upon annealing can be related to the formation of Fe-P complexes with octahedral coordination (as FeP or $FeP_2$) revealed by XAS. The formation of FeP and $FeP_2$ precipitates has been observed in the past in highly Fe doped vapor-phase epitaxy (VPE) and metal-organic chemical-vapor deposition (MOCVD) grown InP samples.[8,9] The presence of Fe-P clusters in these equilibrium grown samples is a confirmation that the FeP and $FeP_2$ configurations are stable in Fe-doped InP. Nonetheless, some significant differences have to be pointed out in our case with respect to VPE or MOCVD grown samples. In particular, in equilibrium growth processes the formation of Fe-P clusters is related to Fe precipitation when it is introduced in concentrations above $10^{17}$ $cm^{-3}$. In our case instead we do not observe the nucleation of Fe-P clusters of large dimensions: it is the displacement of the Fe atoms due to interstitial diffusion that favors the formation of stable Fe-P complexes consisting of few atoms. EXAFS and TEM results have provided a support to this hypothesis. The EXAFS measurements, indeed, have shown that the samples do not show a structural signal beyond the first coordination shell indicating that the local surrounding of Fe is quite disordered beyond the first shell (as it would happen if Fe is never exclusively in an undistorted site) and/or that the compounds are extremely small. Beside this, TEM images did not reveal the presence of Fe-containing clusters confirming that the spatial extent of the Fe-P complexes revealed by XAS measurements is very small (fractions of nanometers, i.e., involving few atoms) being below the TEM sensitivity.

Finally, the changes occurring in the samples upon the

high-temperature annealing treatments and the possible formation of Fe-P complexes have been further supported by the x-ray diffraction results (Fig. 4). The features visible in the strain profile can be explained by the convolution of two effects, which provide strain contributions in opposite directions. First, the presence of a residual concentration of interstitials, not completely recombined upon annealing, produces the expansion of the InP lattice; this effect gives rise to a positive strain contribution which is evident in the whole implantation region.[53] The minimum in the strain profile visible by the Fe peak, instead, is due to the superposition to this positive contribution of a negative strain component whose maximum is in the Fe peak region. The presence of Fe-P complexes can originate this negative contribution. As remarked in Sec. III B, indeed, the Fe-P bond lengths of these complexes are in the range 2.243 and 2.350 Å and are smaller than the In-P bond length in the crystal lattice (2.541 Å). The formation of Fe-P complexes, thus, may produce a shrinkage of the lattice parameter which is more pronounced where the concentration of these complexes is high, that is, very likely, in the region with the maximum iron density. Beside this, a contraction effect can also be induced by the presence of a non-negligible substitutional Fe fraction in the annealed samples, in analogy with the as-implanted samples; again, the maximum effect would coincide with the implanted Fe peak. On the other hand, the presence of a small substitutional fraction cannot be completely excluded on the basis of our PIXE-channeling measurements: a low substitutional fraction, indeed, may be masked by experimental uncertainties as well as by the formation of the Fe-P complexes, whose orientation with respect to the InP host lattice is not known; they may give rise to an enhancement of the Fe signal in channeled directions which masks the presence of an axial minimum due to a substitutional fraction. Moreover, the results of electrical and optical characterizations reported by our group in some recent papers[21–23] demonstrated that in the 600°C annealed samples a fraction of about 10% of the implanted Fe is electrically and optically active, further supporting the hypothesis that a residual substitutional fraction is however present in high-temperature annealed samples. Nonetheless, we believe that the dominant contribution to the lattice contraction in the strain profile is more likely induced by the presence of Fe-P complexes: the residual substitutional Fe concentration is indeed much lower than the total implanted Fe amount eligible for their formation.

## V. CONCLUSION

In this paper we presented a detailed structural investigation of the atomic environment of implanted Fe impurities in InP. The aim was to understand the mechanisms leading to the final location of the iron atoms during the high-temperature implantation process and the subsequent annealing treatments. The investigation has been performed by using a variety of different structural techniques which provided complementary information, in order to obtain an overall picture of the physical processes. In particular, PIXE-channeling and XAS measurements have been extensively employed to study the lattice location of Fe in the InP crystal and its local environment. The picture we can draw on the basis of the obtained results can be summarized as follows. The high-temperature implantation process produces a far-from-equilibrium situation in the as-implanted samples, characterized by a limited damage production due to the local recombination of implant-induced point defects and a very high fraction of Fe atoms incorporated in substitutional positions. During postimplantation thermal treatments the mobility of the residual interstitials which have not completely recombined during the high-temperature implant increases by increasing the annealing temperature; thanks to this, a good crystal reconstruction occurs at low annealing temperatures, while at the highest temperatures the interstitials gain enough energy to coalesce and form the observed secondary extended defects. The diffusion of the interstitials during the annealing process, on the other hand, causes the displacement of Fe atoms from substitutional positions; the mechanism is very likely a kick-out mechanism of the Fe atoms by the mobile interstitials which tend to return in their original sites. Consequently, most of the Fe atoms become visible to the proton beam inside the lattice channels in PIXE-channeling measurements. Beside this, XAS measurements indicate that the displacement of the Fe atoms favors the formation of Fe-P complexes containing few atoms with an increased coordination (octahedral) with respect to the tetrahedral coordination exhibited in the as-implanted samples. Moreover, the limited damage produced in the high-temperature implantation processes and the formation of these Fe-P agglomerates reduce the Fe diffusivity in the samples and stable profiles as a function of the annealing temperature can be obtained, as observed by SIMS measurements.

## ACKNOWLEDGMENTS

This work was partially supported by the ''HeavyFe'' PAIS project of INFM. Financial support of the INFM Synchrotron Radiation Committee for experiments at ESRF is gratefully acknowledged.

*Corresponding author. FAX:+39.049.8277003; Electronic address: cesca@padova.infm.it

[1] S.G. Bishop, *Deep Centers in Semiconductors*, edited by S. Pantelides (Gordon and Breach, New York, 1986).

[2] W.H. Cheng, C.B. Su, K.D. Buehring, C.P. Chien, J.W. Ure, D. Perrachione, D. Renner, K.L. Hess, and S.W. Zehr, Appl. Phys. Lett. **49**, 1415 (1986).

[3] C. Angulo Barrios, S. Lourdudoss, and H. Martinsson, J. Appl. Phys. **92**, 2506 (2002).

[4] O. Kjebon, S. Lourdudoss, B. Hammmarlund, S. Lindgren, M. Rask, P. Ojala, G. Landgren, and B. Broberg, Appl. Phys. Lett. **59**, 253 (1991).

[5] G. Scamarcio, F. Capasso, A.L. Hutchinson, T. Tanbun-Ek, D. Sivco, and A.Y. Cho, Appl. Phys. Lett. **68**, 1374 (1996).

[6] P.B. Klein, J.E. Furneaux, and R.L. Henry, Appl. Phys. Lett. **42**, 638 (1983).
[7] F.S. Shishiyanu, V.G. Gheorghiu, and S.K. Palazov, Phys. Status Solidi A **40**, 29 (1977).
[8] M. Luysberg, R. Gobel, and H. Janning, J. Vac. Sci. Technol. B **12**, 2305 (1994).
[9] S.N.G. Chu, R.A. Logan, N.T. Ha, S. Nakahara, R.F. Karlicek, Jr., and J.A. Grenko, J. Electrochem. Soc. **141**, 242 (1994).
[10] J.P. Donnelly and C.E. Hurwitz, Solid-State Electron. **21**, 475 (1978).
[11] M. Gauneau, H. L'Haridon, A. Rupert, and M. Salvi, J. Appl. Phys. **53**, 6823 (1982).
[12] J. Cheng, S.R. Forrest, B. Tell, D. Wilt, B. Schwartz, and P.D. Wright, J. Appl. Phys. **58**, 1780 (1985).
[13] J. Cheng, S.R. Forrest, B. Tell, D. Wilt, B. Schwartz, and P.D. Wright, J. Appl. Phys. **58**, 1787 (1985).
[14] S.J. Pearton, Mater. Sci. Rep. **3**, 313 (1990).
[15] S.A. Schwarz, B. Schwartz, T.T. Sheng, S. Singh, and B. Tell, J. Appl. Phys. **58**, 1698 (1985).
[16] H. Ullrich, A. Knecht, D. Bimberg, H. Kräutle, and W. Schlaak, J. Appl. Phys. **70**, 2604 (1991).
[17] H. Ullrich, A. Knecht, D. Bimberg, H. Kräutle, and W. Schlaak, J. Appl. Phys. **72**, 3514 (1992).
[18] J. Vellanki, R.K. Nadella, M.V. Rao, O.W. Holland, D.S. Simons, and P.H. Chi, J. Appl. Phys. **73**, 1126 (1993).
[19] A. Gasparotto, A. Carnera, C. Frigeri, F. Priolo, B. Fraboni, A. Camporese, and G. Rossetto, J. Appl. Phys. **85**, 753 (1999).
[20] E. Wendler, T. Opfermann, and P.I. Gaiduk, J. Appl. Phys. **82**, 5965 (1997).
[21] A. Gasparotto, A. Carnera, A. Paccagnella, B. Fraboni, F. Priolo, E. Gombia, and R. Mosca, Appl. Phys. Lett. **75**, 668 (1999).
[22] B. Fraboni, A. Gasparotto, F. Priolo, and G. Scamarcio, Appl. Phys. A: Mater. Sci. Process. **A73**, 35 (2001).
[23] M. Troccoli, G. Scamarcio, B. Fraboni, F. Priolo, and A. Gasparotto, Semicond. Sci. Technol. **15**, L1 (2000).
[24] *X-ray Absorption*, edited by D.C. Konigs Berger and R. Prints (Wiley, New York, 1988).
[25] F. D'Acapito, S. Mobilio, G. Battaglin, E. Cattaruzza, F. Gonella, F. Caccavale, P. Mazzoldi, and J.R. Regnard, J. Appl. Phys. **87**, 1819 (2000).
[26] G.A. Antypas, Appl. Phys. Lett. **37**, 64 (1980).
[27] S. Pascarelli, F. Boscherini, F. D'Acapito, J. Hrdy, C. Meneghini, and S. Mobilio, J. Synchrotron Radiat. **3**, 147 (1996).
[28] S. Takagi, Acta Crystallogr. **15**, 1311 (1962).
[29] D. Taupin, Bull. Soc. Fr. Mineral. Cristallogr. **87**, 469 (1964).
[30] C. Frigeri, A. Carnera, and A. Gasparotto, Appl. Phys. A: Mater. Sci. Process. **62**, 65 (1996).
[31] A. Gasparotto, T. Cesca, G. Mattei, V. Rampazzo, B. Fraboni, F. Boscherini, F. Priolo, E. C. Moreira, G. Ciatto, and F. D'Acapito (unpublished).
[32] G.A. Waychunas, M.A. Apted, and G.E. Brown, Jr., Phys. Chem. Miner. **10**, 1 (1983).
[33] M. Wilke, F. Farges, P.E. Petit, G.E. Brown, Jr., and F. Martin, Am. Mineral. **86**, 714 (2001).
[34] M. Newville, P. Livins, Y. Yacoby, E.A. Stern, and J.J. Rehr, Phys. Rev. B **47**, 14 126 (1993).
[35] S.I. Zabinski, J.J. Rehr, A. Ankudinov, R.C. Albers, and M.J. Eller, Phys. Rev. B **52**, 2995 (1995).
[36] A.L. Ankudinov, B. Ravel, J.J. Rehr, and S.D. Conradson, Phys. Rev. B **58**, 7565 (1998).
[37] G. Ciatto, F. D'Acapito, B. Fraboni, F. Boscherini, N. El Habra, T. Cesca, A. Gasparotto, E.C. Moreira, and F. Priolo, Nucl. Instrum. Methods Phys. Res. B **200**, 100 (2003).
[38] H. Fjellvag, A. Kjekshus, and A.F. Andresen, Acta Chem. Scand., Ser. A **40**, 227 (1986).
[39] E. Dahl, Acta Chem. Scand. **23**, 2677 (1969).
[40] K.M. Yu, W. Walukiewicz, L.Y. Chan, E.E. Haller, J.M. Jaklevic, and C.M. Hanson, J. Appl. Phys. **74**, 86 (1993).
[41] T. Maruyama, T. Hasegawa, N. Komuro, H. Yamada, W. Ohtsuka, K. Akimoto, Y. Kitajima, K. Maeda, and E. Yagi, J. Appl. Phys. **86**, 5993 (1999).
[42] D.S. Gemmell, Rev. Mod. Phys. **46**, 129 (1974).
[43] B. Bech Nielsen, J.U. Andersen, and S.J. Pearton, Phys. Rev. Lett. **60**, 321 (1988).
[44] L.C. Feldman, J.W. Mayer, and S.T. Picraux, *Materials Analysis by Ion Channeling* (Academic, New York, 1982).
[45] A. Gasparotto, T. Cesca, N. El Habra, B. Fraboni, F. Boscherini, F. Priolo, E.C. Moreira, G. Ciatto, F. D'Acapito, and G. Scamarcio, Mater. Sci. Eng., B **91-92**, 503 (2002).
[46] U. Wahl, A. Vantomme, and G. Langouche, Phys. Rev. Lett. **84**, 1495 (2000).
[47] A.M. Mazzone, Phys. Status Solidi A **95**, 149 (1986).
[48] L.A. Christel and J.F. Gibbons, J. Appl. Phys. **52**, 5050 (1981).
[49] R.A. Brown, O. Kononchuk, G.A. Rozgonyi, S. Koveshnikov, A.P. Knights, P.J. Simpson, and F. Gonzalez, J. Appl. Phys. **84**, 2459 (1998).
[50] S.J. Pearton, J.S. Williams, K.T. Short, S.T. Johnson, D.C. Jacobsen, J.M. Poate, J.M. Gibson, and D.O. Boerma, J. Appl. Phys. **65**, 1089 (1989).
[51] B. Tuck, J. Phys. D **18**, 557 (1984).
[52] H. Zimmermann, U. Gosele, and T.Y. Tan, Appl. Phys. Lett. **62**, 75 (1993).
[53] M. Servidori, R. Angelucci, F. Cembali, P. Negrini, S. Solmi, P. Zaumseil, and U. Winter, J. Appl. Phys. **61**, 1834 (1987).